



### **Science Arts & Métiers (SAM)**

is an open access repository that collects the work of Arts et Métiers Institute of Technology researchers and makes it freely available over the web where possible.

This is an author-deposited version published in: <https://sam.ensam.eu>  
Handle ID: <http://hdl.handle.net/10985/21465>

#### **To cite this version :**

S. D. SALEHI, M. A. RASTAK, M. M. SHOKRIEH, Regis KUBLER, Laurent BARRALLIER - Full-Field Measurement of Residual Stresses in Composite Materials Using the Incremental Slitting and Digital Image Correlation Techniques - Experimental Mechanics - Vol. 60, n°9, p.1239-1250 - 2020

Any correspondence concerning this service should be sent to the repository

Administrator : [scienceouverte@ensam.eu](mailto:scienceouverte@ensam.eu)



# Full-Field Measurement of Residual Stresses in Composite Materials Using the Incremental Slitting and Digital Image Correlation Techniques

S.D. Salehi<sup>1</sup> · M.A. Rastak<sup>1</sup> · M.M. Shokrieh<sup>1</sup> · L. Barrallier<sup>2</sup> · R. Kubler<sup>2</sup>

## Abstract

**Background** The slitting method is a widely used destructive technique for the determination of residual stresses. Because of the rich data content of the full-field methods, optical techniques such as digital image correlation (DIC) are replacing strain gages for surface measurements.

**Objective** The objective of the current paper is to overcome the difficulties that arise in using the DIC technique combined with the slitting method. The present noise, low signal-to-noise ratio, and systematic errors are the main impediments to the use of DIC in the slitting method.

**Methods** An approach based on the eigenstrain concept was exploited to ascertain the optimum region of interest (ROI) for the analysis. After that, a robust procedure was implemented to utilize the DIC method while excluding the rigid body motion and rotation artifacts from the obtained displacements.

**Results** Different slitting steps may cause dissimilar rigid body motions and rotations of the specimen. The proposed method was able to eliminate all of these different shears and stretches in the images simultaneously. The slitting experiment was conducted on a symmetric cross-ply composite specimen, and the slit progressed down to half the thickness. Although some rigid body motions were large, the method managed to exclude all of them for eight slitting steps.

**Conclusion** A comparison made between the results of the current method and those of the strain gage technique shows that they are in acceptable agreement with each other, and this full-field method can be extended to smaller scales or other destructive techniques.

**Keywords** Residual stresses · Laminated composites · Incremental slitting · Digital image correlation

## Introduction

Among the destructive residual stress measurement techniques, the hole-drilling [1, 2] and slitting [3] methods are two of the most popular ones, each having benefits over the other in some ways. Both methods are still being widely used as reliable

measurement techniques to ascertain the existing residual stresses within mechanical parts. The lower sensitivity of the slitting method to noise and data errors along with its ability to acquire residual stresses throughout the whole thickness makes it advantageous over its alternatives, especially while interacting with thick specimens. Moreover, its implementation is fast and straightforward, and one can repeat its empirical procedure for mechanical parts readily [4, 5]. The slitting method has been successfully extended to layered and composite materials [6], and utilizing pulse functions or piecewise polynomials resolves impediments to the use of this method for materials containing discontinuous residual stress fields [7]. In recent years, eigenstrain as the source of the residual stresses has also been utilized to obtain the residual stresses for both isotropic [8, 9] and composite materials [10, 11].

---

✉ M. M. Shokrieh  
Shokrieh@iust.ac.ir

<sup>1</sup> Composites Research Laboratory, Center of Excellence in Experimental Solid Mechanics and Dynamics, School of Mechanical Engineering, Iran University of Science and Technology, Tehran 16846-13114, Iran

<sup>2</sup> MSMP Laboratory, Arts et Métiers, 2, Cours des Arts et Métiers, 13617 Aix-en-Provence, France

As measurement devices and instruments developed over the last century, residual stress determination techniques and computational methods advanced simultaneously. More precise strain gages have replaced the mechanical extensometers, and recently, optical methods have attracted much attention [12]. Unlike experiments involving strain gages, which require significant specimen preparation and measurement time, noncontacting optical measurements can be performed much more quickly [2]. Although the precision of optical measurements is modest, the rich data content obtained by them compensates for these shortcomings [13]. Since digital image correlation (DIC) is not among the interferometric techniques that are highly sensitive to vibrations, it is not confined to optical laboratories and can be exploited in industries with less strict mechanical stability requirements [14].

In the DIC method, two photos are taken before (reference) and after (deformed) the deformation to determine the displacements of the region of interest (ROI) [15, 16]. Early residual stress evaluation procedures utilized the obtained full-field data similar to the methods based on techniques used for strain gage measurements [17–19]. However, this approach neglects the rich available measurement redundancy and limits its data usage to a small subset of the whole optical data. Moreover, seeking the best strategy to exploit the data used necessitates significant human guidance to conduct the data selection [20]. Since the signal-to-noise ratio of the optical methods is modest, using techniques based on the strain gage methods might result in high sensitivity to measurement artifacts, which will eventually lead to considerable errors in the computed residual stresses. To overcome these downsides, some methods have been developed to utilize the full-field measurement characteristics of the optical techniques. These full-field techniques have been successfully developed and implemented for electronic speckle pattern interferometry (ESPI) measurements [13, 21]. Further studies [14, 20, 22] put the full-field DIC technique into practice and obtained the residual stresses of isotropic and orthotropic specimens. The full-field DIC techniques have several advantages over their alternatives, such as minimizing the need for human interaction in the computation procedure, giving the displacements in multiple directions [20], and covering a large range of length scales spanning from microns to meters [23, 24].

To date, few investigations on the residual stress determination of materials using the slitting method and DIC analysis have been conducted [25–27]. The methods proposed in these papers do not present a full-field approach to utilize all the available data and assume that the small misalignments between the mounted specimen and the installed camera are controlled and therefore do not affect the measured displacements or strains. The present paper aims to offer a robust approach that takes into consideration all of the slitting increment displacements and obtains the residual stress distribution throughout the thickness. Moreover, thanks to the great data

richness available from optical images, we present a method that excludes the relative motion artifacts from the measured displacements to improve the accuracy of the final results.

## Residual Stress Determination Via Incremental Slitting Coupled with DIC Measurements

The destructive residual stress computation approaches are based on material removal and displacement measurements of regions that undergo elastic strain relaxation. In the slitting method, the material is removed from the part incrementally, and the corresponding relieved strains are recorded generally at the strain gage locations, which can be positioned at the top of the specimen close to the slit or the bottom of the coupon in front of the cut [6]. The top strain gage is most sensitive to the initial slit increments, and its recorded data reach a plateau after a few increments while simultaneously losing their sensitivity to the material removal steps that take place in the deep thicknesses of the specimen. However, the strain gage positioned at the back of the coupon is sensitive to all of the slitting increments that occur throughout the specimen thickness. Despite the location of the mounted strain gage, the existing residual stresses within the material could be obtained using equation (1).

$$\{A\} = [C]^{-1} \{\varepsilon\} \quad (1)$$

In equation (1),  $A_i$  denote the unknown coefficients of the basis functions,  $C_{ij}$  are the compliance matrix elements and  $\varepsilon_j$  are the measured elastic strains up to the  $j$ -th slitting increment. Once the unknown coefficients are determined, the residual stress field can be obtained easily. One can follow the same approach for the residual stress calculation via DIC coupled to the slitting by assuming a virtual strain gage at the bottom or top of the specimen and measuring the displacements of the back or top surface after each slitting step. Eventually, the strains can be computed at the virtual strain gage location, and the unknown coefficients of the basis functions can be obtained as in the strain gage method. The virtual strain gage method obtained from DIC, however, suffers from several drawbacks:

- Using numerical differentiation to estimate the strains from the surface displacements worsens the calculated residual stresses notoriously;
- Choosing the strain gage size and location requires much human guidance;
- The virtual strain gage method disregards the rich available data of surface displacements obtained by DIC;
- Compared to strain gages, the precision of the measured displacements and strains is not very high, and the computed residual stresses experience extreme data-error amplifications.

The presented downsides underscore the necessity to offer an alternative approach to avoid these limitations. In the present research, a robust and accurate full-field method that excludes these drawbacks is developed and assessed.

## Region of Interest Determination and Finite Element Modeling

The covered area in the images captured by the camera plays an imperative role in determining the residual stresses. If the elastic strain relief occurs merely in a small portion of the ROI, the image will mostly capture the insignificant rigid body motions, and if the camera zooms into a very small area, the details of the deformation pattern after the material removal will be disregarded. Therefore, it is wise to consider the ROI as efficiently as possible (i.e., large enough to include the deformation pattern and small enough to exclude the unimportant regions). Using the eigenstrain-based method [11, 28], the region in which the composite material undergoes elastic strain relaxation could be determined. The classical lamination theory (CLT) [29] aids in determining the residual stress distribution through the thickness of the part but is unable to ascertain the redistribution of the residual stress field after the material removal or the state of displacements, elastic strains, and stresses near the free surfaces. This objective is accomplished by exploiting finite element analysis and the eigenstrain-based method. Therefore, for a mechanical part of which the eigenstrain field is known, the aforementioned fields are ascertained conveniently.

Consider a cross-ply  $[90_4/0_4]_s$  laminated composite that is cooled from the curing temperature to ambient conditions. All of the layers contract in the longitudinal and transverse directions as the temperature of the composite part decreases. The equivalent thermal expansion coefficients in the longitudinal ( $\alpha_x$ ) and transverse ( $\alpha_y$ ) directions are obtained using the micromechanical relationships and thermal expansion coefficients of fibers and resin [30]. These relationships are presented in equation (2).

$$\alpha_1 = \frac{\alpha_f E_f V_f + \alpha_m E_m V_m}{E_f V_f + E_m V_m},$$

$$\alpha_2 = \alpha_f V_f + \alpha_m V_m + \frac{\nu_f E_m - \nu_m E_f}{\frac{E_m}{V_f} + \frac{E_f}{V_m}} (\alpha_f - \alpha_m) \quad (2)$$

with  $V_f + V_m = 1$

where  $f$  and  $m$  signify the fiber and matrix, respectively. Moreover,  $\alpha$ ,  $V$ ,  $E$ , and  $\nu$  represent the coefficients of thermal expansion, volume fraction, Young's modulus, and Poisson's ratio, respectively. In the finite element analysis, one can simply set these thermal expansion coefficients for the on-axis directions

of each layer. After a fictitious thermal load, one obtains the residual stresses and elastic strains before and after the slitting increments. In Fig. 1(a), the released elastic strains at the back surface when the slit progresses up to half the specimen thickness are shown. The released elastic strains are not dependent on the lateral direction ( $y$ -axis) and are functions only of the longitudinal direction ( $x$ -axis) and the depth of the slit. Notably, the colored area is the most important region of the back surface owing to the considerable released elastic strains, whereas the changes in the other regions are negligible. As a result, the ROI should include this zone to enable observing and recording the meaningful displacements of this area. Since the values of the released strains are very low in the black zone, the material undergoes mostly rigid body motions, and the meaningful displacements are negligible. The eigenstrain-based approach can also be replaced with the supplemental stress analysis [31] approach, which addresses the relieved tractions at the faces of the slit, and their results correlate with each other very well [28]. Figure 1(b, c) shows the model that was used in this analysis, where mesh size refinement is applied near the slit. Moreover, the symmetry about the middle of the slit is used to reduce the runtime of the solution.

The ROI was obtained via the different steps of the slitting method, and it was found that although the ROI does not change drastically, it is always better to choose an ROI according to the last slitting step. In Fig. 2, the normalized relieved strains of different slitting steps are shown. In this figure,  $h$  indicates the depth of the slit, and  $t_1$  is the thickness of the specimen. Here, it can be seen that ROIs obtained according to different slitting steps are not notably different, but we used the last step, which had a larger width, to define the ROI for the whole experiment.

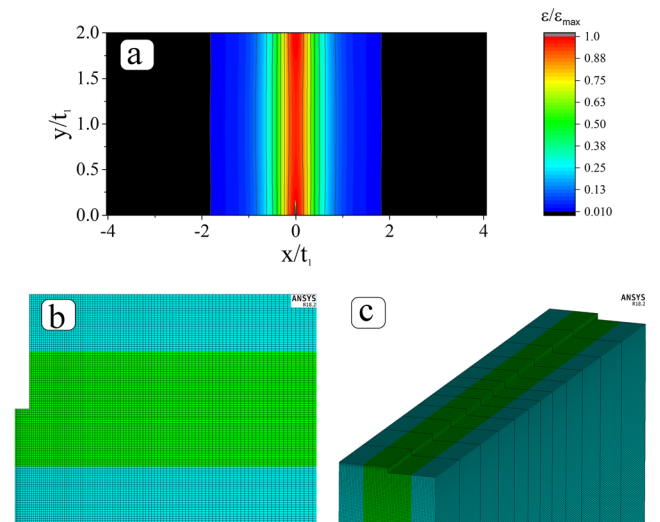


**Fig. 1** (a) Normalized relieved elastic strains in the x-direction at the back surface (finite element simulation); (b) side view of the FE model; (c) isometric view of the FE model

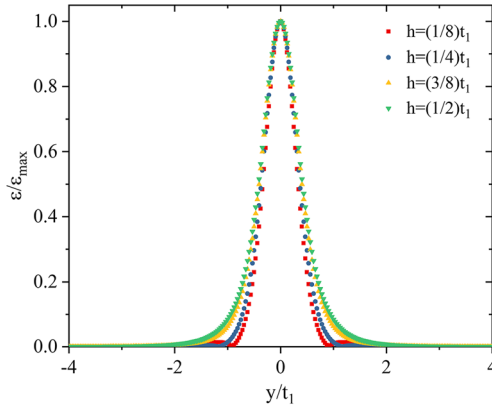


**Fig. 2** The normalized relieved strains at different slitting steps used to obtain the region of interest

### Full-Field Residual Stress Determination

Using the eigenstrain field to reproduce the residual stress field within the specimen, the important area at the back surface of the slitted part was approximately obtained. Now, assuming the slitting procedure to consist of several increments and the displacements of the middle of the specimen, which is exactly in front of the slit, to be zero, one can write the relationships between the displacements of an arbitrary point at the back surface of the specimen and the unknown coefficients of the residual stress as follows:

$$\{d\} = [G]\{A\} \quad (3)$$

Regarding the basis functions as pulse functions and the slitting to consist of 3 steps, one can rewrite equation (3) as follows:

$$\begin{Bmatrix} d_1 \\ d_2 \\ d_3 \end{Bmatrix} = \begin{bmatrix} G_{11} & 0 & 0 \\ G_{21} & G_{22} & 0 \\ G_{31} & G_{32} & G_{33} \end{bmatrix} \begin{Bmatrix} A_1 \\ A_2 \\ A_3 \end{Bmatrix} \quad (4)$$

In these two equations,  $d_i$  represents the measured displacements due to the  $i$ -th slitting increment,  $G_{ij}$  represents the total surface deformation after the  $i$ -th slitting increment, which is caused by the unit stress of the  $j$ -th increment, and  $A_i$  are the unknown coefficients. The matrix  $G$  can be easily computed using finite element analysis, and by multiplying the inverse of  $G$  by the displacement vector, the unknown coefficients of the pulse functions are readily found. In parallel, one can write equation (4) for other points at the back surface of the specimen. Combining these relationships together, one can formulate equation (5) for all of the measured displacements simultaneously.

$$\begin{bmatrix} G_{11}^1 & 0 & 0 \\ G_{21}^1 & G_{22}^1 & 0 \\ G_{31}^1 & G_{32}^1 & G_{33}^1 \\ \vdots & \vdots & \vdots \\ G_{11}^r & 0 & 0 \\ G_{21}^r & G_{22}^r & 0 \\ G_{31}^r & G_{32}^r & G_{33}^r \end{bmatrix} \begin{Bmatrix} A_1 \\ A_2 \\ A_3 \end{Bmatrix} = \begin{Bmatrix} d_1^1 \\ d_2^1 \\ d_3^1 \\ \vdots \\ d_1^r \\ d_2^r \\ d_3^r \end{Bmatrix} \quad (5)$$

In equation (5), the superscripts denote the points at which the deformation is being measured, and  $r$  denotes the maximum amount of data used. In this equation, the matrix  $G$  is highly overdetermined, and the best-fit solution can be found using the least-squares method. Equation (6) finds the best-fit unknown coefficients.

$$([G]^T[G])^{-1}[G]^T\{d\} = \{A\} \quad (6)$$

The presented equation regards all the data holistically and is by far less prone to random errors in the measurements. Therefore, the modest signal-to-noise ratio of the DIC measurements is compensated using this approach. In the slitting method, while utilizing the back surface for measurements, the pattern is not damaged throughout the test because the cuts are performed on the other side, and in contrast to the presented hole-drilling method [20], there is no need to avoid faulty data near the hole or slit edge.

If the residual stresses of a specimen are to be acquired using the strain gage method, the elements of the compliance matrix are obtained by considering the strains at the strain gage location, and the rest of the solution is similar to equation (1). Here, since a large amount of data is received at each slitting increment, the curve fitting can be used to reproduce the magnitudes of  $G_{mn}^p$  of a point  $p$  of coordinates  $(x, y)$  at the back surface of the specimen. Apart from the free edges of the slit, the displacements and residual stresses of the composite part can be assumed constant along the lateral direction ( $y$ -axis) of the specimen (Fig. 3). Therefore, the displacements at the back surface are merely

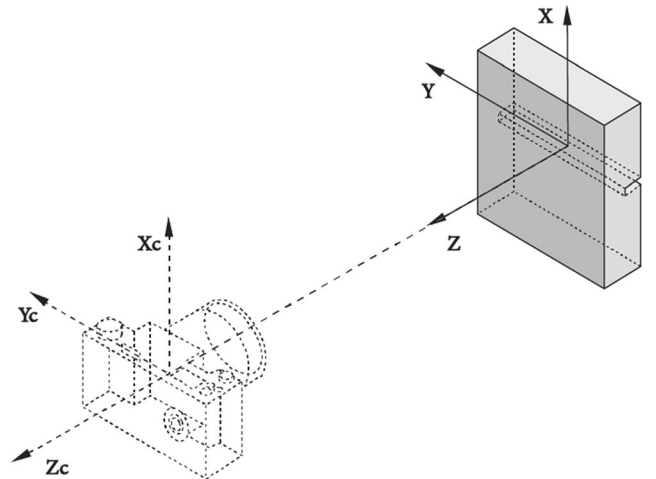


**Fig. 3** Schematic of the DIC-assisted incremental slitting experiment



functions of the longitudinal direction (x-axis). As a result, the elements of the  $\mathbf{G}$  in equation (5) can be written as follows.

$$G_{mn}^p = G_{mn}(x, y) = G_{mn}(x) = \sum_{j=1}^q B_{mnj} P_j(x) \quad (7)$$

In equation (7),  $B_{mnj}$  are the fitted curve coefficients, and  $P_j(x)$  are the basis functions computed in the curve fitting procedure. Consequently, the elements of the matrix  $\mathbf{G}$  and fitted curve coefficients for the  $i$ -th slitting increment and  $j$ -th unit pulse can be easily calculated. In addition to the random errors that occur in the measurements, systematic errors can be present owing to poor installation of the camera or specimen. Therefore, rigid body motions and rotations might occur during the experiment and hence should be excluded from the raw data; otherwise, the final results, which are quite sensitive to the systematic errors, will be negatively affected.

Systematic errors may occur according to Fig. 4. Rigid body motions are shown in Fig. 4(a)-(c), while the remaining subfigures exhibit rigid body rotations. The rigid body motion in (a) moves the specimen in the x-direction and causes unique rigid body motions for all the points. The rigid body motion in Fig. 4(b) moves all points in the y-direction, which does not change the x-displacements. The rigid body motion in (c) is more severe than the other two rigid body motions and causes a scaling change, thereby resulting in axial stretch along the x- and y-directions. The rigid body rotation in (d) results in shear for the longitudinal displacements, which means that the displacements in the x-direction will be linearly dependent on the y-coordinate. The rigid body rotation in (e) imposes some axial stretch along

the x-direction. Moreover, the rigid body rotation in (f) produces shear and stretch in both directions. As stated above, the displacements along the y-direction are not important and can be neglected in the analysis, as far from the edges, stresses and strains can be assumed to be constant.

Similar to the formulation presented for the hole-drilling method by Schajer et al. [20], the displacements at the back surface regarding the rigid body motions and rotations can be formulated for the incremental slitting method. Considering the rigid body motions, stretch, and shear, the displacements along the x-axis can be written as:

$$d_i(x) = \sum_{j=1}^r G_{ij}(x) A_{j1} = \sum_{j=1}^i G_{ij}(x) A_{j1} + A_{i2} + x A_{i3} + y A_{i4} \quad (8)$$

In this equation,  $A_{i1}$  are coefficients associated with the unit pulses,  $A_{i2}$  denote the unknown rigid body motions of different slitting increments, and  $A_{i3}$  and  $A_{i4}$  signify the coefficients related to the stretch and shear along the x-axis at different slitting steps, respectively. In this equation, all of the errors introduced by rigid body motions and rotations are accounted for at the same time; it is worth noting that the combined effects of these artifacts are included in equation (8), and one cannot simply separate the effects of cases (a)-(f) readily. As written in equations (4 and 5),  $\mathbf{G}$  is a lower triangular matrix, and as a result,  $j$  never exceeds  $i$  in the summation. The systematic errors related to specimen motions are taken into account in equation (8), and one can rewrite equation (5) to account for these artifacts. To help visualize these ideas, equation (9) is written for a special case where three slitting steps are performed on a specimen and the displacements are recorded at five points.

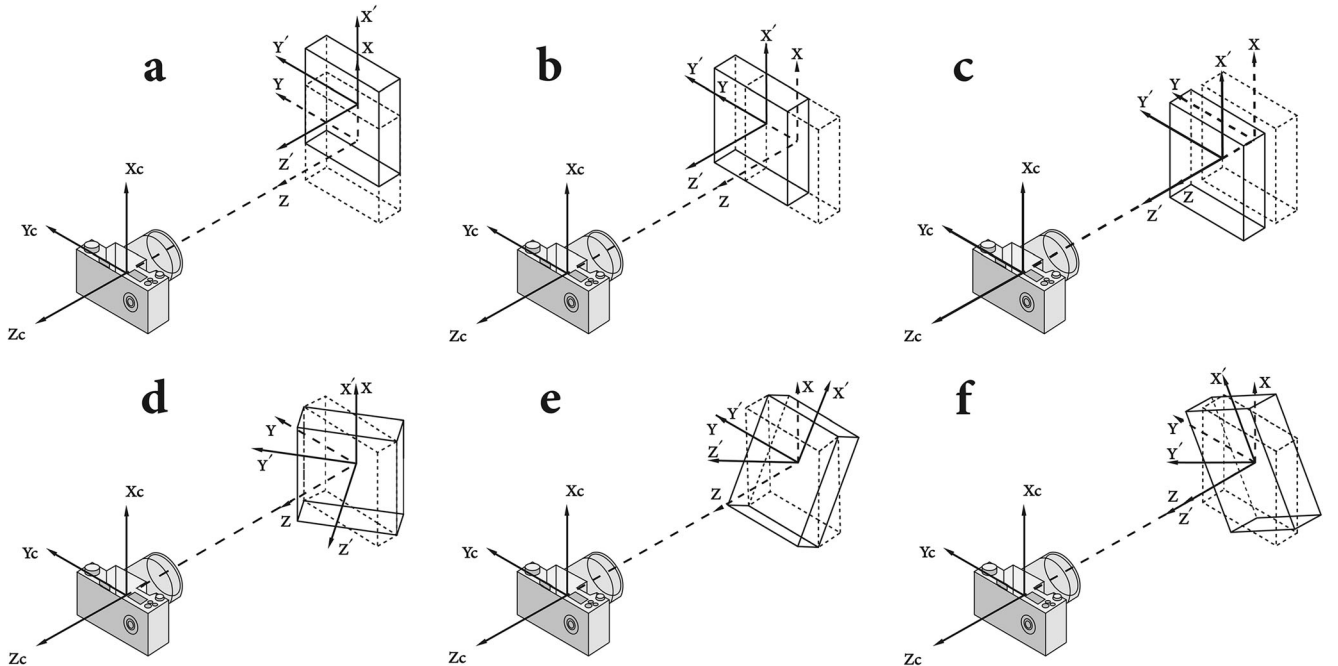


Fig. 4 The relative rigid body motions and rotations: (a-c) rigid body motions and (d-f) rigid body rotations

$$\begin{bmatrix}
G_{11}(x_1) & 1 & x_1 & y_1 & 0 & 0 & 0 & 0 & 0 & 0 & 0 & 0 \\
G_{21}(x_1) & 0 & 0 & 0 & G_{22}(x_1) & 1 & x_1 & y_1 & 0 & 0 & 0 & 0 \\
G_{31}(x_1) & 0 & 0 & 0 & G_{32}(x_1) & 0 & 0 & 0 & G_{33}(x_1) & 1 & x_1 & y_1 \\
\hline
G_{11}(x_2) & 1 & x_2 & y_2 & 0 & 0 & 0 & 0 & 0 & 0 & 0 & 0 \\
G_{21}(x_2) & 0 & 0 & 0 & G_{22}(x_2) & 1 & x_2 & y_2 & 0 & 0 & 0 & 0 \\
G_{31}(x_2) & 0 & 0 & 0 & G_{32}(x_2) & 0 & 0 & 0 & G_{33}(x_2) & 1 & x_2 & y_2 \\
\hline
G_{11}(x_3) & 1 & x_3 & y_3 & 0 & 0 & 0 & 0 & 0 & 0 & 0 & 0 \\
G_{21}(x_3) & 0 & 0 & 0 & G_{22}(x_3) & 1 & x_3 & y_3 & 0 & 0 & 0 & 0 \\
G_{31}(x_3) & 0 & 0 & 0 & G_{32}(x_3) & 0 & 0 & 0 & G_{33}(x_3) & 1 & x_3 & y_3 \\
\hline
G_{11}(x_4) & 1 & x_4 & y_4 & 0 & 0 & 0 & 0 & 0 & 0 & 0 & 0 \\
G_{21}(x_4) & 0 & 0 & 0 & G_{22}(x_4) & 1 & x_4 & y_4 & 0 & 0 & 0 & 0 \\
G_{31}(x_4) & 0 & 0 & 0 & G_{32}(x_4) & 0 & 0 & 0 & G_{33}(x_4) & 1 & x_4 & y_4 \\
\hline
G_{11}(x_5) & 1 & x_5 & y_5 & 0 & 0 & 0 & 0 & 0 & 0 & 0 & 0 \\
G_{21}(x_5) & 0 & 0 & 0 & G_{22}(x_5) & 1 & x_5 & y_5 & 0 & 0 & 0 & 0 \\
G_{31}(x_5) & 0 & 0 & 0 & G_{32}(x_5) & 0 & 0 & 0 & G_{33}(x_5) & 1 & x_5 & y_5
\end{bmatrix}
\begin{Bmatrix}
A_{11} \\
A_{12} \\
A_{13} \\
A_{14} \\
A_{21} \\
A_{22} \\
A_{23} \\
A_{24} \\
A_{31} \\
A_{32} \\
A_{33} \\
A_{34}
\end{Bmatrix}
=
\begin{Bmatrix}
d_1(x_1) \\
d_2(x_1) \\
d_3(x_1) \\
d_1(x_2) \\
d_2(x_2) \\
d_3(x_2) \\
d_1(x_3) \\
d_2(x_3) \\
d_3(x_3) \\
d_1(x_4) \\
d_2(x_4) \\
d_3(x_4) \\
d_1(x_5) \\
d_2(x_5) \\
d_3(x_5)
\end{Bmatrix} \quad (9)$$

By exploiting equations (6 and 9), the best fit solution can be achieved to exclude systematic artifacts and to obtain more accurate results. In addition to the previous methods that eliminated the relative motions of the destructive methods that contained a single step, the present formulation excludes the artifacts of several slitting steps all at once.

The eigenstrain-based method can also be put into practice to obtain the residual stresses of the specimen and is similar to the conventional method. Once the eigenstrain field is determined, this field is applied to another FE model to achieve the residual stresses. The whole procedure to obtain the residual stresses is described in [11]. Equation (10) can be rewritten similar to equation (8) for the eigenstrain-based solution as follows:

$$d_i(x) = \sum_{j=1}^r \Delta H_{ij}(x) A_{j1} + A_{i2} + x A_{i3} + y A_{i4} \quad (10)$$

where  $\Delta H_{ij}(x)$  represents the total surface deformation after the  $i$ -th slitting increment, which is caused by the unit eigenstrain applied to the  $j$ -th increment. Although the compliance matrix in the conventional method is a lower triangular, all components of the matrix  $\Delta H$  possess nonzero values.

We observed earlier that the present method is a reliable tool for excluding the random errors that occur in the experimental procedure. However, a series-truncation technique can also be employed to reduce the sensitivity of the final solutions to the available noise in the measurements. In this approach, the number of unknowns is reduced, while the number of measurements or equations remains the same as before. As a result, overdetermination of the matrices  $\mathbf{G}$  and  $\Delta \mathbf{H}$  occurs, and the final results are more robust. Therefore, without

changing the number of measurements, the number of pulse functions is reduced. The whole procedure for both the conventional and eigenstrain-based methods is described in [11], and the same approach can be employed for the current problem to mitigate the sensitivity of the final results to the available data errors in the measurements.

In the procedure proposed by Schajer and Rickert [32], the measurement and computational approaches were changed so that the stresses are calculated in terms of the deformation alternation during each material removal increment. This change benefits the solution in two ways: first, the time between the reference and deformation images is reduced. Therefore, the phase unwrapping quality is improved. Moreover, the associated mathematical relationship between deformations and residual stresses is better conditioned and offers more stable results. The same approach can be used here; however, this procedure mostly improves the final results by reducing the time between the deformation and reference images, and since the measurements are recorded at the back surface of the specimen, these measurements retain their sensitivity to the slit increments from the first to the last steps. Consequently, this procedure mainly benefits the solution by improving optical correlation and enhancing image quality. Hence, for the aforementioned problem, the deformations of consecutive increments can be added up to use equation (9), or one can utilize equation (11) to use the mathematical procedure in its differential form. Here, the stretch and shear of each step are expressed with respect to the previous slitting step, which also has the differential form. The displacements along the  $z$ -direction due to the induced bending after the slitting steps are disregarded in this analysis and assumed to be negligible.

$$\begin{bmatrix}
G_{11}(x_1) & 1 & x_1 & y_1 & 0 & 0 & 0 & 0 & 0 & 0 & 0 \\
G_{21}(x_1)-G_{11}(x_1) & 0 & 0 & 0 & G_{22}(x_1) & 1 & x_1 & y_1 & 0 & 0 & 0 \\
G_{31}(x_1)-G_{21}(x_1) & 0 & 0 & 0 & G_{32}(x_1)-G_{22}(x_1) & 0 & 0 & 0 & G_{33}(x_1) & 1 & x_1 & y_1 \\
\hline
G_{11}(x_2) & 1 & x_2 & y_2 & 0 & 0 & 0 & 0 & 0 & 0 & 0 \\
G_{21}(x_2)-G_{11}(x_2) & 0 & 0 & 0 & G_{22}(x_2) & 1 & x_2 & y_2 & 0 & 0 & 0 \\
G_{31}(x_2)-G_{21}(x_2) & 0 & 0 & 0 & G_{32}(x_2)-G_{22}(x_2) & 0 & 0 & 0 & G_{33}(x_2) & 1 & x_2 & y_2 \\
\hline
G_{11}(x_3) & 1 & x_3 & y_3 & 0 & 0 & 0 & 0 & 0 & 0 & 0 \\
G_{21}(x_3)-G_{11}(x_3) & 0 & 0 & 0 & G_{22}(x_3) & 1 & x_3 & y_3 & 0 & 0 & 0 \\
G_{31}(x_3)-G_{21}(x_3) & 0 & 0 & 0 & G_{32}(x_3)-G_{22}(x_3) & 0 & 0 & 0 & G_{33}(x_3) & 1 & x_3 & y_3 \\
\hline
G_{11}(x_4) & 1 & x_4 & y_4 & 0 & 0 & 0 & 0 & 0 & 0 & 0 \\
G_{21}(x_4)-G_{11}(x_4) & 0 & 0 & 0 & G_{22}(x_4) & 1 & x_4 & y_4 & 0 & 0 & 0 \\
G_{31}(x_4)-G_{21}(x_4) & 0 & 0 & 0 & G_{32}(x_4)-G_{22}(x_4) & 0 & 0 & 0 & G_{33}(x_4) & 1 & x_4 & y_4 \\
\hline
G_{11}(x_5) & 1 & x_5 & y_5 & 0 & 0 & 0 & 0 & 0 & 0 & 0 \\
G_{21}(x_5)-G_{11}(x_5) & 0 & 0 & 0 & G_{22}(x_5) & 1 & x_5 & y_5 & 0 & 0 & 0 \\
G_{31}(x_5)-G_{21}(x_5) & 0 & 0 & 0 & G_{32}(x_5)-G_{22}(x_5) & 0 & 0 & 0 & G_{33}(x_5) & 1 & x_5 & y_5
\end{bmatrix}
\begin{Bmatrix}
A_{11} \\ A_{12} \\ A_{13} \\ A_{14} \\ A_{21} \\ A_{22} \\ A_{23} \\ A_{24} \\ A_{31} \\ A_{32} \\ A_{33} \\ A_{34}
\end{Bmatrix}
=
\begin{Bmatrix}
d_1(x_1) \\ d_2(x_1)-d_1(x_1) \\ d_3(x_1)-d_2(x_1) \\ d_1(x_2) \\ d_2(x_2)-d_1(x_2) \\ d_3(x_2)-d_2(x_2) \\ d_1(x_3) \\ d_2(x_3)-d_1(x_3) \\ d_3(x_3)-d_2(x_3) \\ d_1(x_4) \\ d_2(x_4)-d_1(x_4) \\ d_3(x_4)-d_2(x_4) \\ d_1(x_5) \\ d_2(x_5)-d_1(x_5) \\ d_3(x_5)-d_2(x_5)
\end{Bmatrix} \quad (11)$$

## Experimental Procedure

The method proposed in the previous part offers several advantages, such as mitigating the sensitivity of the final results to random and systematic errors. To evaluate the practicality of the method, one must empirically investigate it. In this section, the specimen preparation, camera setup adjustments, and slitting experiment are discussed.

## Specimen Fabrication

A cross-ply laminated composite with a  $[90_4/0_4]_s$  lay-up was fabricated by using the hand lay-up method. The materials used were carbon fibers with ML506 epoxy resin and HA-11 hardener. The ML506 epoxy resin was mixed with the HA-11 hardener, and the mixture was stirred for 5 mins at 1000 rpm. Additionally, the mixture was placed under a vacuum to remove the air bubbles. To ensure the uniformity of the thickness, a rigid planar plate was in contact with the top face of the laminated composite during the curing process. The laminated composite was cured under atmospheric pressure for 6 h at 100 °C and was followed by another process at 120 °C for the same period. Thereafter, the temperature was reduced very slowly to ambient conditions. The mechanical properties of the unidirectional plies are listed in Table 1. The thickness of each layer was approximately 0.4 mm according to optical measurements. Ultimately, after the laminated composites were cut, rectangular specimens with dimensions of  $65 \times 95 \times 6.4$  mm were tested in the present research.

## Digital Image Correlation

Digital image correlation (DIC) is a noncontacting optical technique that is combined with different experimental setups to ascertain the displacements of the ROI using a single or multicamera system; the former is used in this paper to obtain the two-dimensional surface deformations of the object. 2D full-field displacement analysis is a robust tool that has been used to obtain the residual stresses in recent studies [15]. Here, the same approach is put into practice to obtain the residual stresses across the thickness of the laminate.

Furthermore, providing an appropriate speckle pattern at the ROI is an integral part of DIC analysis. By calculating the transformation parameters for images of different slitting steps, one can obtain the displacement vector for small elements named facets [33]. It is also essential to create a random pattern on the surface, and the pattern may contain a white background with black dots or vice versa. The speckle pattern that is used in this analysis is shown in Fig. 5.

## Camera Shooting Settings

Other aspects toward achieving satisfactory results in the DIC test are dependent on the camera shooting settings. One has to make careful adjustments to the ISO, shutter speed, and aperture settings. To take images with proper quality, digital noises should be minimized, and the brightness of images should be carefully controlled (images that are not too dark nor too bright). To fulfill these requirements, the ISO, shutter speed, and aperture were considered to be 200, 1/50 s, and F/2.8,

**Table 1** The mechanical properties of the unidirectional ply [11]

$E_1$ (GPa)	$E_2$ (GPa)	$G_{12}$ (GPa)	$\nu_{12}$	Fiber volume fraction (%)	Layer thickness (mm)
116.6	10.7	3.8	0.31	50	0.4



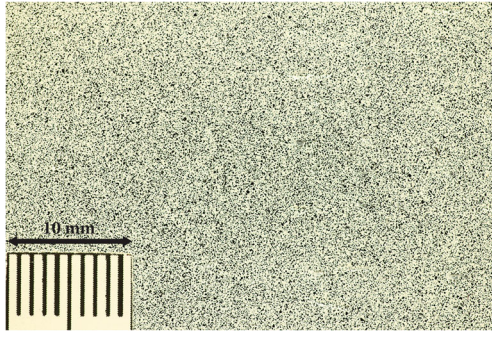


**Fig. 5** The speckle pattern sprayed on the back surface of the composite specimen

respectively. Additionally, a camera with a maximum resolution of 18 MP ( $5184 \times 3456$ ) was installed on a tripod to take photos before and after each slitting increment.

### Incremental Slitting Method

The composite specimen was mounted on a fixture to carry out the incremental slitting method. In cross-ply laminated composites, if the slit is parallel to the fibers of the upper layers, higher elastic strains will be relieved at the back surface of the specimen, where the displacements are measured [7, 34]. Moreover, small misalignments in bonding the strain gage or planar rotation of the specimen with respect to the camera will not cause very high errors in the final results [35]. Therefore, the direction of the slit was considered to be parallel to the upper-layer fibers. The thickness of the blade, spindle rotation speed, and feed rate were set to 0.8 mm, 2000 rpm, and 40 mm/min, respectively. The experimental setup is illustrated in Fig. 6(a, b). It is also worth mentioning that to stabilize the measured displacements at the back surface of the specimen, after each slitting increment, the spindle was turned off, and eventually, the image was taken after two minutes. The slitting consisted of eight increments, and each slitting increment increased the depth of the slit by 0.4 mm. Due to the symmetry of the specimen, the slit progressed down to

the middle of the thickness, and the residual stresses were assumed to be symmetric with respect to the mid-surface.

Prior to conducting the DIC-assisted experiment, the composite laminate was cut in half to perform another slitting experiment involving a strain gage for comparison. The same machining settings were used for the conventional experiment, except that a strain gage was utilized instead of a speckle pattern to record the relieved strains. A BHF350-3HA strain gage with a gage length of 3.5 mm, supplied by Juxing Co., was bonded to the back surface of the composite specimen in front of the slit, and the excitation voltage was set to 5 V with a sampling rate of 3 per second.

### Results and Discussion

Before evaluating the proposed method experimentally, it is worthwhile to verify it numerically; using the eigenstrain approach, thermal coefficients were set according to equation (2) to induce the residual stresses in a cross-ply laminated composite with a  $[90_4/0_4]_s$  lay-up. Therefore, the displacements at the back surface can be computed after creating the slit conveniently. These displacements were recorded at all nodes of the back surface and for all of the slitting increments. To imitate the real shear and stretch artifacts in the simulations, errors were added to the true displacements according to equation (12). In this equation,  $d'_i(x)$  denote the simulated displacements, which include different types of errors,  $d_i(x)$  are the true displacements that are obtained via the FE analysis,  $a$  determines the intensity of the noise or random error in the data,  $random$  is a function that outputs normally distributed data between  $-1$  to  $1$ , and  $b$  and  $c$  are coefficients that determine the intensity of the stretch and shear effects, respectively. The parameter  $i$ , which corresponds to the number of slitting steps, is included in this equation to produce different magnitudes of error for different slitting steps. These parameters were utilized according to Table 2. Because of the presence of the random function in equation (12), we may obtain a different set of outputs for each run. Therefore, for each value

**Fig. 6** The experimental setup: (a) the real setup; (b) a schematic of the experimental setup

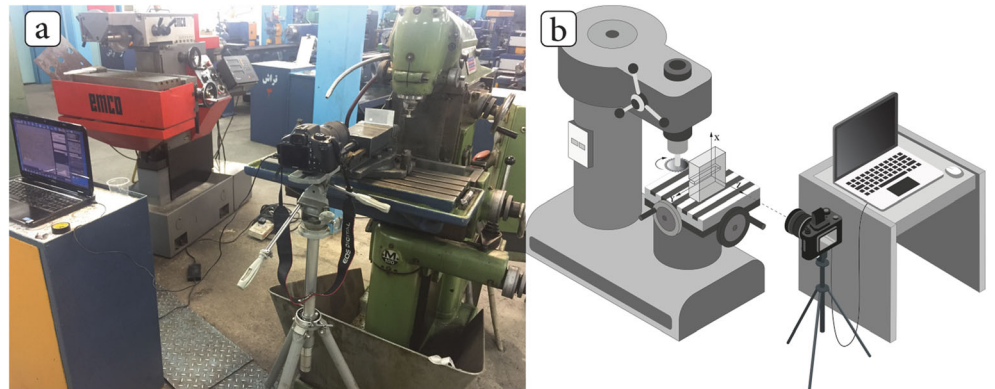


**Table 2** The results of the simulation of the DIC-assisted incremental slitting containing relative motion artifacts

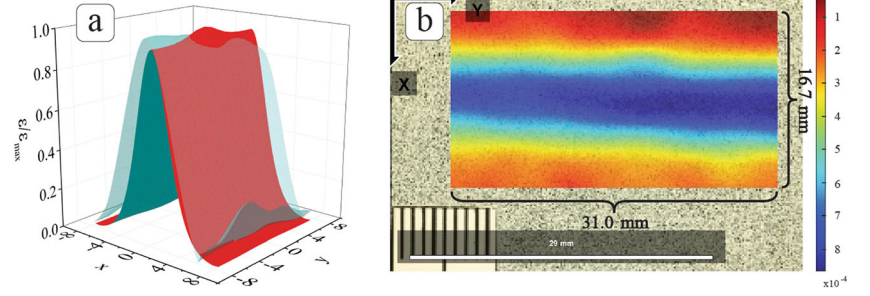
a	b	c	Type	A <sub>11</sub> (Pa×10 <sup>6</sup> )	A <sub>12</sub> (m)	A <sub>13</sub> (1 × 10 <sup>-6</sup> )	A <sub>14</sub> (1 × 10 <sup>-6</sup> )
1 × 10 <sup>-5</sup>	1 × 10 <sup>-4</sup>	2 × 10 <sup>-4</sup>	Mean	1.13×10 <sup>1</sup>	1.00	1.00×10 <sup>2</sup>	2.00×10 <sup>2</sup>
			STD	2.46×10 <sup>1</sup>	6.18×10 <sup>-7</sup>	1.75×10 <sup>1</sup>	2.68×10 <sup>1</sup>
1 × 10 <sup>-6</sup>	1 × 10 <sup>-4</sup>	2 × 10 <sup>-4</sup>	Mean	1.57×10 <sup>1</sup>	1.00	1.00×10 <sup>2</sup>	2.00×10 <sup>2</sup>
			STD	2.17	5.55×10 <sup>-8</sup>	1.44	3.14
1 × 10 <sup>-7</sup>	1 × 10 <sup>-4</sup>	2 × 10 <sup>-4</sup>	Mean	1.53×10 <sup>1</sup>	1.00	9.99×10 <sup>1</sup>	2.00×10 <sup>2</sup>
			STD	2.68×10 <sup>-1</sup>	5.90×10 <sup>-9</sup>	1.94×10 <sup>-1</sup>	3.19×10 <sup>-1</sup>
1 × 10 <sup>-8</sup>	1 × 10 <sup>-4</sup>	2 × 10 <sup>-4</sup>	Mean	1.53×10 <sup>1</sup>	1.00	1.00×10 <sup>2</sup>	2.00×10 <sup>2</sup>
			STD	2.35×10 <sup>-2</sup>	5.82×10 <sup>-10</sup>	1.76×10 <sup>-2</sup>	2.84×10 <sup>-2</sup>
				A <sub>21</sub> (Pa×10 <sup>6</sup> )	A <sub>22</sub> (m)	A <sub>23</sub> (1 × 10 <sup>-6</sup> )	A <sub>24</sub> (1 × 10 <sup>-6</sup> )
1 × 10 <sup>-5</sup>	1 × 10 <sup>-4</sup>	2 × 10 <sup>-4</sup>	Mean	2.33×10 <sup>1</sup>	2.00	1.99×10 <sup>2</sup>	4.01×10 <sup>2</sup>
			STD	5.37×10 <sup>1</sup>	5.35×10 <sup>-7</sup>	1.73×10 <sup>1</sup>	3.03×10 <sup>1</sup>
1 × 10 <sup>-6</sup>	1 × 10 <sup>-4</sup>	2 × 10 <sup>-4</sup>	Mean	1.38×10 <sup>1</sup>	2.00	2.00×10 <sup>2</sup>	4.00×10 <sup>2</sup>
			STD	5.02	5.68×10 <sup>-8</sup>	1.84	2.99
1 × 10 <sup>-7</sup>	1 × 10 <sup>-4</sup>	2 × 10 <sup>-4</sup>	Mean	1.49×10 <sup>1</sup>	2.00	2.00×10 <sup>2</sup>	4.00×10 <sup>2</sup>
			STD	6.40×10 <sup>-1</sup>	5.48×10 <sup>-9</sup>	1.95×10 <sup>-1</sup>	3.17×10 <sup>-1</sup>
1 × 10 <sup>-8</sup>	1 × 10 <sup>-4</sup>	2 × 10 <sup>-4</sup>	Mean	1.48×10 <sup>1</sup>	2.00	2.00×10 <sup>2</sup>	4.00×10 <sup>2</sup>
			STD	5.80×10 <sup>-2</sup>	5.67×10 <sup>-10</sup>	1.76×10 <sup>-2</sup>	3.22×10 <sup>-2</sup>
				A <sub>31</sub> (Pa×10 <sup>6</sup> )	A <sub>32</sub> (m)	A <sub>33</sub> (1 × 10 <sup>-6</sup> )	A <sub>34</sub> (1 × 10 <sup>-6</sup> )
1 × 10 <sup>-5</sup>	1 × 10 <sup>-4</sup>	2 × 10 <sup>-4</sup>	Mean	-1.92×10 <sup>1</sup>	3.00	2.99×10 <sup>2</sup>	5.99×10 <sup>2</sup>
			STD	5.71×10 <sup>1</sup>	5.56×10 <sup>-7</sup>	2.21×10 <sup>1</sup>	3.19×10 <sup>1</sup>
1 × 10 <sup>-6</sup>	1 × 10 <sup>-4</sup>	2 × 10 <sup>-4</sup>	Mean	-1.34×10 <sup>1</sup>	3.00	3.00×10 <sup>2</sup>	6.00×10 <sup>2</sup>
			STD	5.78	5.00×10 <sup>-8</sup>	2.09	3.24
1 × 10 <sup>-7</sup>	1 × 10 <sup>-4</sup>	2 × 10 <sup>-4</sup>	Mean	-1.44×10 <sup>1</sup>	3.00	3.00×10 <sup>2</sup>	6.00×10 <sup>2</sup>
			STD	6.80×10 <sup>-1</sup>	5.14×10 <sup>-9</sup>	2.02×10 <sup>-1</sup>	3.03×10 <sup>-1</sup>
1 × 10 <sup>-8</sup>	1 × 10 <sup>-4</sup>	2 × 10 <sup>-4</sup>	Mean	-1.43×10 <sup>1</sup>	3.00	3.00×10 <sup>2</sup>	6.00×10 <sup>2</sup>
			STD	6.58×10 <sup>-2</sup>	5.69×10 <sup>-10</sup>	2.01×10 <sup>-2</sup>	3.50×10 <sup>-2</sup>
				A <sub>41</sub> (Pa×10 <sup>6</sup> )	A <sub>42</sub> (m)	A <sub>43</sub> (1 × 10 <sup>-6</sup> )	A <sub>44</sub> (1 × 10 <sup>-6</sup> )
1 × 10 <sup>-5</sup>	1 × 10 <sup>-4</sup>	2 × 10 <sup>-4</sup>	Mean	-1.54×10 <sup>1</sup>	4.00	4.01×10 <sup>2</sup>	8.00×10 <sup>2</sup>
			STD	4.15×10 <sup>1</sup>	5.91×10 <sup>-7</sup>	2.33×10 <sup>1</sup>	3.38×10 <sup>1</sup>
1 × 10 <sup>-6</sup>	1 × 10 <sup>-4</sup>	2 × 10 <sup>-4</sup>	Mean	-1.59×10 <sup>1</sup>	4.00	4.00×10 <sup>2</sup>	8.00×10 <sup>2</sup>
			STD	3.97	6.00×10 <sup>-8</sup>	1.97	2.90
1 × 10 <sup>-7</sup>	1 × 10 <sup>-4</sup>	2 × 10 <sup>-4</sup>	Mean	-1.56×10 <sup>1</sup>	4.00	4.00×10 <sup>2</sup>	8.00×10 <sup>2</sup>
			STD	4.52×10 <sup>-1</sup>	5.40×10 <sup>-9</sup>	2.21×10 <sup>-1</sup>	2.84×10 <sup>-1</sup>
1 × 10 <sup>-8</sup>	1 × 10 <sup>-4</sup>	2 × 10 <sup>-4</sup>	Mean	-1.55×10 <sup>1</sup>	4.00	4.00×10 <sup>2</sup>	8.00×10 <sup>2</sup>
			STD	4.68×10 <sup>-2</sup>	4.93×10 <sup>-10</sup>	2.38×10 <sup>-2</sup>	3.15×10 <sup>-2</sup>

of  $a$  that shows the intensity of the random errors, we ran the code 100 times and obtained the averages and standard deviations shown in Table 2. The simulated slitting consisted of four steps, and the slit progressed down to the middle of the thickness. As a result, each slitting increment was equal to the thickness of two layers of the composite specimen. Since the simulated experiment consisted of four slitting increments and 2000 nodes at the back surface, in this analysis, the number of rows of the matrix  $\mathbf{G}$  was  $2000 \times 4$ , and the number of columns, which determines the number of unknowns, was  $4 \times 4$ .

$$d'_i(x) = d_i(x) + a \text{ random}() + x i b + y i c + i \quad (12)$$

The results of the DIC-assisted slitting simulation are presented in Table 2. The results are exhibited for different magnitudes of random errors and each range of these errors, and the problem was solved 100 times to obtain the standard deviation of the solutions. In Table 2, it is obvious that by reducing the noise intensity in the raw data, the final results are stabilized. The typical root-mean-square (*RMS*) of the present

**Fig. 7** (a) A comparison between the FEM (red) and DIC (blue) normalized strains; (b)  $\varepsilon_{xx}$  strain contours of the region of interest at a slitting depth of 3.2 mm (half the thickness of the laminate)



noise in the DIC analysis is approximately 0.02 pixels [20, 36]. Typical errors lie between the second and third rows of random errors; thus, in a real test, the residual stresses will have satisfactory precision. Therefore, for random errors in the typical range, the present procedure excludes the rigid body motions and rotations completely and provides acceptable results.

Figure 7(a) shows a comparison between the prediction of the eigenstrain-based approach and the DIC results. The red curve (FEM results) shows the relieved strains at the back surface, which are normalized by their maximum magnitude. The blue surface shows the results of the DIC test, in which numerical differentiation is used to produce the strains for different points; the strains are normalized by their maximum magnitude as well. The eigenstrain-based approach or supplemental stress analysis has the potential to predict the region in which the material undergoes residual stress relief. Therefore, one can use these approaches to predict the desired ROI before conducting the test. This concept was utilized earlier to find the repeated slitting distance of some specimens [28]. The differences between these curves stem from the errors of the DIC analysis and rough estimation of the eigenstrain field within the composite material. In Fig. 7(b), it is shown that the ROI was chosen carefully before conducting the experiments.

Using the proposed full-field method according to equations (6 and 9), the residual stresses were computed.

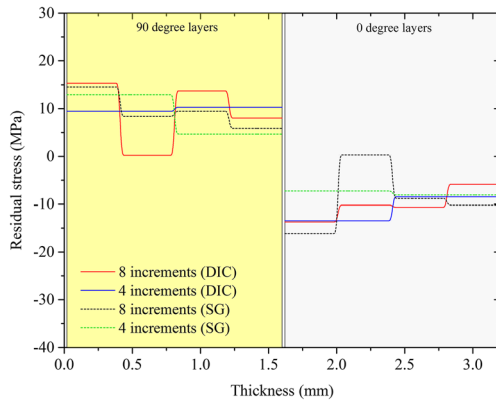


**Fig. 8** Comparison between the results of the present method and those of the strain gage method (for 4 increments, the series truncation method is used)

Figure 8 exhibits the calculated residual stresses and shows the differences between the results of the DIC and strain gage measurements. The method that was used to compute the residual stresses by utilizing the strain gage data was performed according to [11], which is straightforward. The dashed lines demonstrate the residual stresses obtained by the strain gage measurements, while the solid lines illustrate the residual stresses computed by the full-field DIC measurements. In this figure, it is notable that although the signal-to-noise ratio of the strain gages is far better than the DIC measurements, the rich data content of the DIC measurements makes up for the low precision of the measurements, and the final results have acceptable precision and stability. In both techniques, when series truncation is used and the number of pulse functions is reduced from 8 to 4, the results become more stable, but their corresponding resolution decreases at the same time. The results agree well with the strain gage solution, especially for the truncated series solution, which displays the credibility of the proposed full-field method. Additionally, the prediction of the precision of the outcomes of the full-field DIC method according to Table 2 is accurate, which shows that the practicality of these full-field techniques can be assessed beforehand.

To see the effect of the exclusion of relative body motion artifacts on the final results, it is helpful to compare the current method (where  $\mathbf{G}$  is computed according to equation (9)) with the method in which  $\mathbf{G}$  is calculated according to equation (5). In Fig. 9, the stresses that are obtained by these methods are

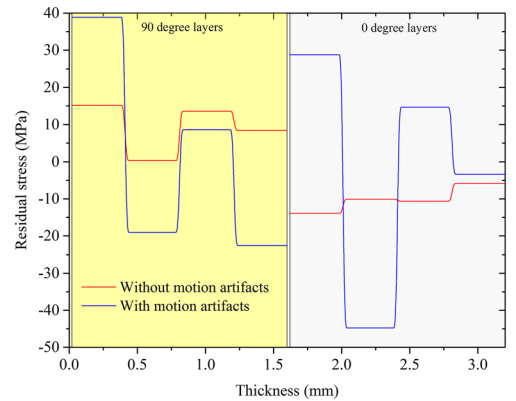


**Fig. 9** The effect of the rigid body motion and rotation artifacts on the final results

depicted. It can be seen that the blue line stresses that are obtained by using equation (5) are noisy and do not make sense, since in the 90-degree layers, the stresses should be positive, while in the 0-degree layers, they should be negative. The existing rigid body motions and rotations in the displacements cause the final answers to deviate from the more accurate case, which is exhibited in red. The higher the magnitudes of the rigid body motions and rotations, the worse the final residual stresses become.

For this specific problem, the stresses obtained by using equation (11) were worse than the stresses obtained by using equation (9) and were not reported. This poor performance stems from the fact that the method of Schajer and Rickert [32] can improve the cases in which the diagonal elements on the matrix  $\mathbf{G}$  start to decrease as the depth of the slit increases. This physically means that their method improves cases in which the sensitivity of the surface to the slit progression drops drastically. For the case in which the displacements are measured at the back surface, the sensitivity of the displacements to the slitting steps is maintained during the experiment. This formulation is presented as a possible use for the case where the displacements are measured at the top surface, with the displacements losing their sensitivity to the slit progression.

The proposed full-field method was successful in determining the residual stress field of composite materials not only because of the very large amount of data, which helped to diminish the effects of the random errors on the final results, but also because of the exclusion of the systematic artifacts in the measurements. For each set of measurement data (i.e., each image), these artifacts were removed, and all of them were eliminated at once automatically utilizing the least-squares approach. To clearly illustrate how the method

removes these artifacts, the measured displacements of the last image are shown in Fig. 10.

In Fig. 10(a-d), the blue surface exhibits the displacements of which these artifacts are removed, which we call “true” in this section. Figure 10(a) shows the raw displacements versus the true data, highlighting the considerable improvements that are made in the analysis. In Fig. 10(b), the brown surface shows the displacements in which the rigid body motions are not removed. This figure highlights the fact that no matter how great the rigid body motions are in the system, the proposed method disregards them completely. The brown surface in Fig. 10(c) shows the present shears in the measured displacements. As was assumed previously, by moving along the y-axis, no change should be observed in the displacements, and the blue surface rectifies this problem noticeably. The brown and blue surfaces in Fig. 10(d) are very close to each other, which shows that the stretches in the measurements were not very high to considerably influence the final results. These artifacts were eliminated in the same way for all of the slitting steps, and the filtered displacements were implemented in the analysis to assure the validity of the computed stresses.

## Conclusions

In this research, a full-field residual stress measurement was developed whereby the residual stresses through the thickness were obtained using the DIC technique and incremental slitting method. The computational technique made use of the large extent of data available from the optical images to diminish the effects of the modest deformation sensitivity of the DIC technique on the final results. Additionally, this method did not require any human guidance except for choosing the region of interest, which was carefully selected using the eigenstrain-based method or supplemental stress analysis. Moreover, the present approach exploits a large quantity of data to rectify the relative body motion artifacts; the effects of the image shifts, shears, and stretches of all images were removed mathematically. Although the shear effects and rigid body motions were high for some slitting steps, this method eliminated all of them successfully to guarantee the validity of the final results. Since the pulse functions were used in this analysis, the results were prone to amplification of the data error and noise; therefore, the series truncation method was used to diminish these artifacts. Consequently, the results with lower numbers of pulse functions were more stabilized but possessed lower resolution. The present method can be extended to the incremental hole-drilling and ring-core methods using the multiaxial deformation capability of the DIC.

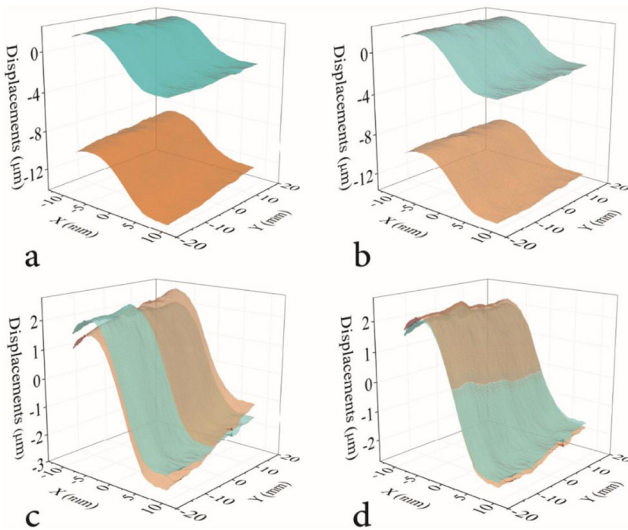


**Fig. 10** The existing relative motions in the measured displacements and the true displacements



## Compliance with Ethical Standards

**Conflict of Interest** The authors declare that they have no conflicts of interest.

## References

- Schajer G (1988) Measurement of non-uniform residual stresses using the hole-drilling method. Part I-stress calculation procedures. *J Eng Mater Technol* 110:338–343
- Schajer GS, Whitehead PS (2013) Hole drilling and ring coring, *Practical Residual Stress Measurement Methods*, 29–64
- Prime MB (1999) Residual stress measurement by successive extension of a slot: the crack compliance method. *Appl Mech Rev* 52: 75–96
- Hill MR (2013) The slitting method, *Practical residual stress measurement methods*, 89–108
- Lee MJ, Hill MR (2007) Intralaboratory repeatability of residual stress determined by the slitting method. *Exp Mech* 47:745–752
- Shokrieh M, Akbari S (2014) Measuring residual stresses in composite materials using the slitting/crack compliance method, in: *Residual Stresses in Composite Materials*, Elsevier, pp. 121–151
- Shokrieh M, Akbari S, Daneshvar A (2013) A comparison between the slitting method and the classical lamination theory in determination of macro-residual stresses in laminated composites. *Compos Struct* 96:708–715
- Cheng W (2000) Measurement of the axial residual stresses using the initial strain approach. *J Eng Mater Technol* 122:135–140
- DeWald AT, Hill MR (2009) Eigenstrain-based model for prediction of laser peening residual stresses in arbitrary three-dimensional bodies part 1: model description. *J Strain Analysis Eng Design* 44: 1–11
- Prime MB, Hill MR (2004) Measurement of fiber-scale residual stress variation in a metal-matrix composite. *J Compos Mater* 38: 2079–2095
- Salehi S, Shokrieh M (2019) Residual stress measurement using the slitting method via a combination of eigenstrain, regularization and series truncation techniques. *Int J Mech Sci* 152:558–567
- Nelson D (2010) Residual stress determination by hole drilling combined with optical methods. *Exp Mech* 50:145–158
- Schajer GS, Steinzig M (2005) Full-field calculation of hole drilling residual stresses from electronic speckle pattern interferometry data. *Exp Mech* 45:526–532
- Baldi A (2014) Residual stress measurement using hole drilling and integrated digital image correlation techniques. *Exp Mech* 54:379–391
- Harrington J, Schajer GS (2017) Measurement of structural stresses by hole-drilling and DIC. *Exp Mech* 57:559–567
- Pan B, Qian K, Xie H, Asundi A (2009) Two-dimensional digital image correlation for in-plane displacement and strain measurement: a review. *Meas Sci Technol* 20:062001
- Nelson D, Makino A, Schmidt T (2006) Residual stress determination using hole drilling and 3D image correlation. *Exp Mech* 46:31–38
- Lord JD, Penn D, Whitehead P (2008) The application of digital image correlation for measuring residual stress by incremental hole drilling, in: *Applied Mechanics and Materials*, Trans Tech Publ, pp. 65–73
- Baldi A, Bertolino F (2007) Sensitivity analysis of full field methods for residual stress measurement. *Opt Lasers Eng* 45: 651–660
- Schajer G, Winiarski B, Withers P (2013) Hole-drilling residual stress measurement with artifact correction using full-field DIC. *Exp Mech* 53:255–265
- Winiarski B, Withers PJ (2010) Mapping residual stress profiles at the micron scale using FIB micro-hole drilling, In: *Applied Mechanics and Materials*, Trans Tech Publ, pp. 267–272
- Baldi A (2014) Residual stress analysis of orthotropic materials using integrated digital image correlation. *Exp Mech* 54:1279–1292
- Winiarski B, Schajer G, Withers P (2012) Surface decoration for improving the accuracy of displacement measurements by digital image correlation in SEM. *Exp Mech* 52:793–804
- Salvati E, Sui T, Korsunsky AM (2016) Uncertainty quantification of residual stress evaluation by the FIB–DIC ring-core method due to elastic anisotropy effects. *Int J Solids Struct* 87:61–69
- Blair A, Daynes N, Hamilton D, Home G, Heard P, Hodgson D, Scott T, Shterenlikht A (2009) Residual stress relaxation measurements across interfaces at macro-and micro-scales using slitting and DIC. In: *Journal of Physics: Conference Series*, IOP Publishing, pp. 012078
- Yaowu X, Rui B (2017) Residual stress determination in friction stir butt welded joints using a digital image correlation-aided slitting technique. *Chin J Aeronaut* 30:1258–1269
- Zhu R, Zhang Q, Xie H, Yu X, Liu Z (2018) Determination of residual stress distribution combining slot milling method and finite element approach. *Science China Technol Sci* 61:965–970
- Salehi S, Shokrieh M (2019) Repeated slitting safe distance in the measurement of residual stresses. *Int J Mech Sci* 157–158:599–608
- Cowley KD, Beaumont PW (1997) The measurement and prediction of residual stresses in carbon-fibre/polymer composites. *Compos Sci Technol* 57:1445–1455
- Gay D, Hoa SV (2007) *Composite materials: design and applications*. CRC Press, Boca Raton
- Olson M, Hill M (2018) Two-dimensional mapping of in-plane residual stress with slitting. *Exp Mech* 58:151–166
- Schajer GS, Rickert TJ (2011) Incremental computation technique for residual stress calculations using the integral method. *Exp Mech* 51:1217–1222
- Hagara M, Trebuña F, Pástor M, Huňady R, Lengvarský P (2019) Analysis of the aspects of residual stresses quantification performed by 3D DIC combined with standardized hole-drilling method. *Measurement* 137:238–256
- Ersoy N, Vardar O (2000) Measurement of residual stresses in layered composites by compliance method. *J Compos Mater* 34: 575–598
- Tuttle ME, Brinson HF (1984) Resistance-foil strain-gage technology as applied to composite materials. *Exp Mech* 24:54–65
- Sutton MA (2008) Digital image correlation for shape and deformation measurements, *Springer Handbook of experimental solid mechanics*, 565–600